Lawrence Berkeley National Laboratory

Title

Star Block Copolymers at Homopolymer Interfaces: Conformation and Compatibilization

Permalink

https://escholarship.org/uc/item/1pg8d1xw

Journal

Macromolecules, 56(20)

ISSN

0024-9297

Authors

Chen, Zhan

Steinmetz, Christian

Hu, Mingqiu

et al.

Publication Date

2023-10-24

DOI

10.1021/acs.macromol.3c01139

Peer reviewed

Star Block Copolymers at Homopolymer Interfaces: Conformation and Compatibilization

Zhan Chen[1], ‡ Christian Steinmetz[1], ‡ Mingqiu Hu[1], E Bryan Coughlin[1], Hanyu Wang[2], William T Heller[3], Wim Bras[4], Thomas P. Russell[1,5]

AUTHOR ADDRESS

[1]Department of Polymer Science and Engineering, University of Massachusetts Amherst, Amherst, MA

[2]Center for Nanophase Materials Sciences, Oak Ridge National Laboratory, Oak Ridge, TN

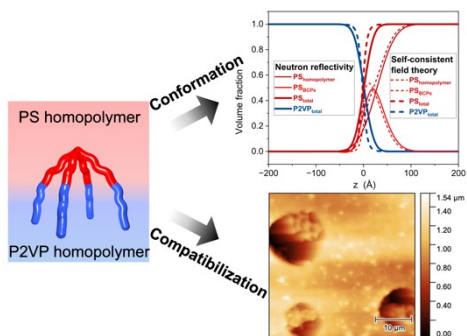[3]Neutron Scattering Division, Oak Ridge National Laboratory, Oak Ridge, TN

[4]Chemical Sciences Division, Oak Ridge National Laboratory, Oak Ridge, TN

[5]Materials Sciences Division, Lawrence Berkeley National Laboratory, Berkeley, CA

For Table of Contents use only

ABSTRACT

Star block copolymers (s-BCPs), comprised of multiple linear diblock copolymers joined at central point, are shown to segregate to the interface between the two immiscible homopolymers that are identical to the blocks of the s-BCPs. The s-BCPs undergo a configurational transition at the interface, with the different blocks of the copolymers being embedded in their respective homopolymers, thereby bridging the interface, and promoting adhesion. A series of 4-arm s-BCPs were synthesized with hydrogenated or deuterated polystyrene (PS/dPS) as the core block and poly(2-vinyl pyridine) (P2VP) as the corona block, which was directly placed at the interface between the two homopolymers. Neutron reflectivity (NR) was used to determine the concentration profiles of the PS homopolymer, s-BCPs core blocks and P2VP total segments under equilibrium. The investigation varies the molecular weights (MW) and the total number of s-BCPs at the interface. Self-consistent-field theory (SCFT) was also employed to calculate the concentration profiles of the components at the interface, which was in excellent agreement with experimental results. The NR showed that the interfacial width between the homopolymers increased with an increasing number of s-BCPs at the interface, up to a saturation limit. Beyond this limit, additional s-BCPs were released into the corona-miscible phase as unimolecular micelles. For comparable interlayer thickness of s-BCPs at the interface, the lower MW s-BCPs generated a broader interface. SCFT analysis suggested that, at the same packing density, the arms of the low MW s-BCPs align more parallel to the interface, while the arm of high MW s-BCPs adopt a more normal orientation, like their linear BCP counterparts. Furthermore, it was also observed the core blocks, constrained by the junction

point, were oriented more parallel and closer to the interface than the corona blocks. The phase behavior of polymer blends showed s-BCP additives can efficiently reduce the domain size, with the low MW yielding smaller domain sizes due to the greater reduction in the interfacial energy and high MW arresting phase separation due to their higher binding energy and a jamming of the interfacial assemblies. Asymmetric double cantilever beam (ADCB) tests showed that s-BCPs promoted adhesion more efficiently than their linear BCP counterparts due to stronger binding energy per molecule, suggesting a more efficient compatibilizer for polymer upcycling. The results from these studies provide fundamental insights into the assembly of s-BCPs at homopolymer interfaces, the reduction of domain size and promotion of adhesion, providing a strategy for the use of s-BCPs as stealth surfactants and universal compatibilizers.

Introduction

The adhesion between dissimilar polymers, between a polymer and a substrate, or in composites of polymer and filler particles, relies primarily on the strength of the interactions between the components at the interface.[1, 2] If the interactions are unfavorable, as is typically seen with two immiscible polymers [3] or a hydrophobic polymer and an oxide layer on a substrate[4] or inorganic filler,[5] the interface represents a weak location and when stress is placed on the system, adhesive failure occurs at the interface, leading to delamination or cavitation. This stress may be due to an external deformation of the system, differences in coefficients of thermal expansion of the components, or differences in the solubility of a fluid or vapor in the components. [2] Regardless of the origin of this mode of failure, it detrimentally affects the

4

ultimate properties of the system, deleteriously impacting use. Multi-layered constructs in microelectronic devices or thin film coatings are two examples where adhesion is critical. [4] Numerous strategies have been developed to circumvent such failure. For example, adhesion promoters can be applied to a substrate where a small molecule, having one part that favorably interacts with the substrate and another that favorably interacts with the coating, can effectively bond the polymer film to a substrate. [6] Block copolymers (BCPs) comprised of two immiscible homopolymers covalently linked at one junction point, or random copolymers that bridge across the interface have been shown to effectively stitch together the interface between two immiscible polymers, improving adhesion to the point where cohesive failure can occurs, in which a crack propagates within one of the polymers, as opposed to at the interface. [7-9]

An emergent area where the adhesion between immiscible polymers is of critical importance is in the upcycling of mixed plastic waste streams. [10, 11] The rapid increase in global plastic production and the massive volume of the resultant post-consumer waste has reached a crisis state that mandates the development of more efficient, universal polymer upcycling strategies. [12] Typical waste streams undergo different degrees of sorting and separation with the hope of limiting the number of components in the sorted streams to be, ideally, one component or two components that are miscible. Subsequent mixing of the components in the melt leads to a single-phased system with properties that depend on those of the polymers that are mixed. This goal has achieved some, but limited, success, as evidenced by the gradual appearance of "made from recycled plastics" labeled products in the marketplace. Not only must the individual polymeric components be considered but, also, the added colorants, fillers, and stabilizers in the original materials introduce an additional level of complexity to any sorting strategy. This

complexity hinders many circular recycling strategies, where chemical, catalytic or enzymatic routes are used to decompose polymers to their original monomers or oligomers that can be used as starting materials for the re-polymerization of new materials. [3, 13, 14]

An alternative approach is upcycling where the components in the waste stream, after a modest level of sorting, are masticated into a blend of multiple immiscible components having phase-separated domains of the individual components with properties that combine those of the original materials. [14] The size scale of the domains is of importance which depends on the temperature and degree of mixing, i.e. residence time in a melt mixer or extruder, which are energy-intensive. [13] The final morphologies are kinetically-trapped and the domain will coarsen to reduce the interfacial area given time and sufficient mobility. [3] To circumvent this problem, interfacially active materials, like block copolymers, could be added or generated *in situ* by a reactive processing, to reduce the interfacial energy, making the generation of smaller domains easier and more stable. [7, 15] However, BCPs will tend to form micelles in one of the polymers, so it must diffuse to the interface and break up before becoming interfacially active, [16] while with reactive processing, for example, using ligands or polymers with complementary end functionality, the reactive species must diffuse to the interface and be spatially co-located to undergo a reaction to form BCPs. [15] While each route is possible, it would be more desirable to have an additive that could be molecularly dispersed in one component that would diffuse to an interface, where it would then exhibit surfactant-like behavior, i.e., behave as stealth surfactants. Once at the interface, the additive would reduce interfacial tension, promote adhesion between two dissimilar materials, and improve the mechanical properties of the mixture. It would also be ideal if such stealth surfactants could be active at multiple interfaces.

One approach to this challenge is to leverage the chain-architecture of copolymers to develop the next generation of compatibilizers.[7, 17-19] We focus on star BCPs (s-BCPs), formed by joining multiple linear BCPs at one junction,[20] that can be molecularly dispersed in the corona-miscible solvent or polymer, regardless of the miscibility of core block with the matrix solvent or polymer.[21, 22] After introducing such s-BCP mixtures to a second immiscible solvent or polymer that is a solvent for the core block, s-BCPs will diffuse to the liquid-liquid interface or polymer-polymer interface and reconfigure, placing the core blocks in the second phase, while keeping the corona blocks solubilized in the initial phase, to reduce the interfacial tension.[23] Consequently, s-BCPs behave as stealth surfactants, unleashing their surfactancy only when in contact with the second immiscible liquid or polymer. We can take this one approach further by considering a mixture of the s-BCPs that have the same corona but different cores that can be molecularly dispersed in the corona-miscible homopolymer phase or solvent. When introducing a second homopolymer, only those s-BCPs with core blocks that favorably interact with the second phase are 'activated' and behave as compatibilizers. The residual s-BCPs will remain dormant. Consequently, such a mixture of s-BCPs can be active and promote adhesion at multiple homopolymer interfaces simultaneously and, therefore, act as universal compatibilizers.

Understanding the equilibrium conformation of s-BCPs at homopolymer interfaces is essential for designing stealth surfactants and universal compatibilizers. This will depend on the architecture of the s-BCPs, i.e., the number of arms, the molecular weights of the arm bock copolymers, the concentration of s-BCPs at the interface. Rather than dispersing the s-BCPs in a homopolymer and allowing diffusion to the interface, we placed the s-BCPs directly at the interface followed by thermal annealing, as was done in numerous studies of BCPs at

homopolymer interface. [24-26] Not only does this expedite the approach to equilibrium for the interfacial assemblies but it also allows placing exact number of s-BCPs at the interface, allowing us to define limits on the number of s-BCPs that could occupy the interface.[24, 27] By quantitatively measuring the variation in the segmental density profiles across a planar interface by neutron reflectivity (NR) and by pairing these measurements with self-consistent field theory (SCFT) calculations, an in-depth understanding of the architecture-governed interfacial behavior of s-BCPs at homopolymer interfaces was obtained. Further, we explored the structure-property relationship by examining the compatibilization efficiency. Here we synthesized a series of 4-arm s-BCPs with hydrogenated or deuterated polystyrene (PS/dPS) as the core blocks and poly(2-vinyl pyridine) (P2VP) as corona blocks, termed as $(S\text{-}b\text{-}V)_4$ or $(dS\text{-}b\text{-}V)_4$.[23, 28] The selective labeling of the homopolymers or blocks of the s-BCPs with deuterium allowed further delineation of the concentration profiles across the interface for different components in the system.[25] When translating the interfacial conformation into compatibilization efficiency, it is important to investigate the domain size and the adhesion strength, since the former reflects the phase separation of blend and the latter affects the stress transfer between domains, and both play significant roles in the mechanical properties of resultant composites. Thin films of polymer blends show that a s-BCP additive can efficiently reduce the domain size, with the low MW s-BCPs having smaller domain sizes, while the high MW s-BCPs exhibit complicated domain shapes. Asymmetric double cantilever beam (ADCB) tests were then used to measure the adhesion and correlate those results with the NR and SCFT results.[8] Surprisingly, the s-BCPs are more efficient than their linear BCP counterparts to promote the adhesion, due, more than likely, to the pinning of the core block to the interface at multiple points.

Results and Discussions

Synthesis of 4-arm star BCPs (s-BCPs)

4-arm s-BCPs comprising PS core and P2VP corona, denoted (S-*b*-V)$_4$, having symmetric volume compositions and different MWs, were synthesized by the grafting-from method using reversible addition-fragmentation chain-transfer (RAFT) polymerization. The analogous 4-arm s-BCPs with dPS as core and P2VP as corona were synthesized by the same method, denoted as (dS-*b*-V)$_4$. The synthetic steps used to prepare the s-BCPs are shown in **Scheme 1.** The characteristics of the s-BCPs synthesized are shown in **Table 1**. We note that two s-BCPs can also join at the arm ends to form bimolecular s-BCPs due to bimolecular termination during RAFT polymerization, [29] as shown in **Scheme 1.** This is evidenced by size exclusion chromatography (SEC) in **Figure S2.** The degree of bimolecular termination is calculated from the Gaussian fitting. The effect of bimolecular termination on the equilibrium conformation of star BCPs at the homopolymer interface will be discussed later. Small angle x-ray scattering (SAXS) profiles of the four s-BCPs in the bulk are shown in **Figure S3.** For the high-MW, s-BCPs show multiple reflections characteristic of a lamellar microdomain morphology indicating that these s-BCPs are strongly microphase-separated. The lower MW s-BCPs show a single, broad, diffuse maximum characteristic, being in the phase-mixed or weakly microphase separated state. The d-spacings corresponding to the peak of the scattering profiles of the high MW s-BCPs are 25.3 nm and 22.6 nm for (dS117-*b*-V153)$_4$ and (S94-*b*-V112)$_4$, and 9.6 nm and 10.6 nm for low MW s-BCPs (dS35-*b*-V66)$_4$ and (S34-*b*-V50)$_4$, respectively.
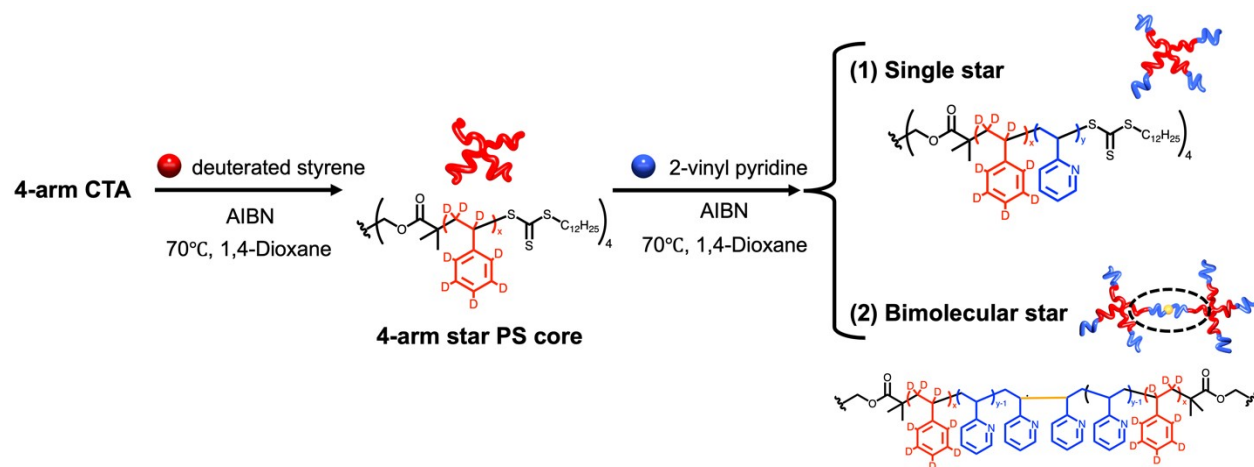
Scheme 1. Synthesis of 4-arm star block copolymers, having deuterated polystyrene (dPS) as core blocks and poly(2-vinyl pyridine) (P2VP) as corona blocks. 4-arm CTA: pentaerythritol tetrakis[2-(dodecylthiocarbonothioylthio)-2-methylpropionate]. The bimolecular star was formed due to the bimolecular termination of two single star BCP radical.

Table 1. Characteristics of 4-arm (d)-PS-*b*-P2VP s-BCPs

Code	(d)-PS block M_n (g/mol) [a]	(d)-PS block DP_n per arm	P2VP block M_n (g/mol) by GPC	P2VP block DP_n per arm by GPC	f_{PS} by GPC	P2VP block DP_n per arm by NMR [b]	f_{PS} by NMR [b]	Total M_n (g/mol)	$Đ$ [c]
(S34-*b*-V50)₄	14000	34	21100	50	0.42	31	0.54	35100	1.15
(dS35-*b*-V66)₄	15500	35	27600	66	0.36	N/A	N/A	43100	1.19
(S94-*b*-V112)₄	39300	94	46900	112	0.48	99	0.51	86200	1.46
(dS117-*b*-V153)₄	52700	117	68300	153	0.44	N/A	N/A	121000	1.29
(fS36-*b*-V18)₄[d]	14800	36	12200	29	0.57	18	0.68	27000	1.16

[a] calculated from size exclusion chromatography (SEC) in dimethylformamide using PS calibration, [b] calculated from volume fractions, [c] determined from size exclusion chromatography (SEC) in dimethylformamide using PS calibration, [d] Fluorescent 4-arm s-BCP, (fS36-*b*-V18), synthesized by copolymerizing tetramethylrhodamine-5-maleimide with styrene.

Width of homopolymer interfaces in the presence of s-BCPs

Neutron reflectivity (NR) was performed on trilayers, denoted as dPS ‖ (dS-*b*-V)$_4$ ‖ P2VP. A thin film of (dPS-*b*-P2VP)$_4$ of known thickness was placed between films of dPS and P2VP homopolymers of known thicknesses. Shown in **Figure 1a** are the neutron reflectivity profiles of the dPS ‖ (dS-*b*-V)$_4$ ‖ P2VP where the MW and interlayer thicknesses were varied. All neutron reflectivity profiles show total external reflection to q$_c$ =0.018 Å^{-1}, which corresponds to critical angle of dPS on the surface. [30] The neutron scattering length densities of PS, dPS and P2VP are 1.39, 6.2 and 1.94 x 10^{-6} Å^{-2}, respectively (determined from critical angle of single homopolymer layer on silicon substrate in NR), while those for the silicon substrate and the native oxide layer are 2.07 and 3.5 x 10^{-6} Å^{-2}. Consequently, with the PS block of the s-BCP residing in the PS homopolymer layer, and the P2VP block of the s-BCP in the P2VP layer, the trilayer effectively reduces to a bilayer of dPS on P2VP with Kiessig fringes characteristic of the combined dPS layer thickness with a decay characteristic of the interfacial width between the dPS and P2VP layers. By increasing interlayer thickness, the Kiessig fringes are damped at smaller q for both low MW and high MW s-BCPs due to increasing interfacial width between the dPS layer and the P2VP layer. With each layer thickness being measured independently by ellipsometry and interferometry, fitting of the NR data requires a single parameter, namely the interfacial width.
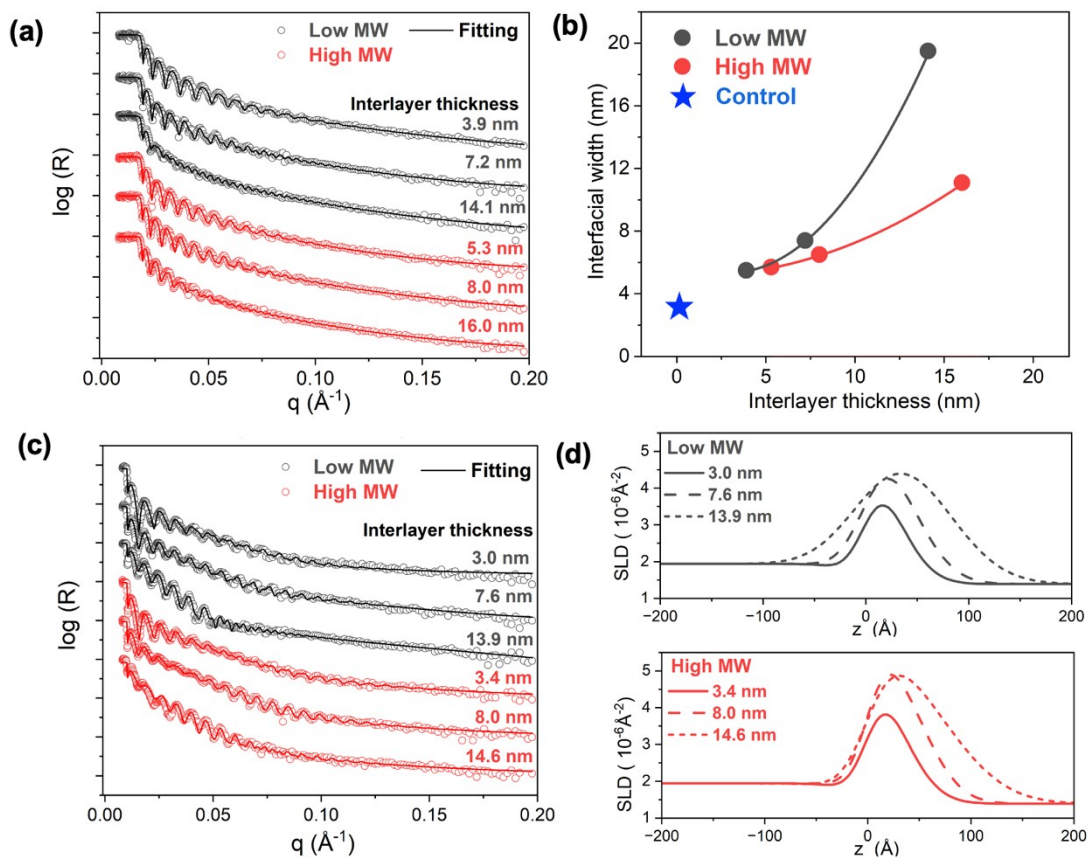
Figure 1. (a) NR profiles of dPS ∥ (dS-*b*-V)$_4$ ∥ P2VP for different (dS-*b*-V)$_4$ MWs and interlayer thicknesses. The reflectivity profiles have been shifted for clarity. **(b)** Interfacial widths (a_I) between dPS and P2VP as a function of the (dS-*b*-V)$_4$ MW and interlayer thickness. **(c)**. NR profiles of PS ∥ (dS-*b*-V)$_4$ ∥ P2VP for different (dS-*b*-V)$_4$ MWs and interlayer thicknesses. The reflectivity profiles have been shifted for clarity. **(d)** Zoomed-in SLD profiles obtained from the fitting of (c) as a function of distance The SLD profiles were shifted horizontally to align the interface at z=0 for comparison. Negative values of z are in the P2VP layer, while positive values of z are in the PS layer.

Given the SLDs profiles that are used to fit the NR data (**Figure S5**), concentration profiles as a function of depth from which the interfacial width between the dPS and P2VP is

determined. The interfacial width a_I in terms of the scattering length density is given by

$$a_I = \frac{\Delta_{SLD}}{\left(dSLD/dz\right)_{SLD=\frac{1}{2}(DPS+P2VP)}}$$ [27, 30]. Without s-BCPs at the interface, the interfacial width between

PS and P2VP homopolymer was determined to be 3.1 nm (**Figure S8**), which is consistent with

the value of 3.4 nm reported previously by Kramer and coworkers. [31] With s-BCPs at interface

(**Figure 1b**), the interfacial width increases to 5.5 nm, 7.4 nm, and 19.5 nm for low MW s-BCPs

with an interlayer thickness of 3.9, 7.2, and 14.1 nm, respectively, and 5.7, 6.5, and 11.1 nm for

high MW s-BCPs with interlayer thicknesses of 5.3, 8.0, and 16.0 nm, respectively.

Consequently, the s-BCPs are seen to reconfigure and assemble at the interface with the PS core

in the PS homopolymer layer and the P2VP corona in the P2VP homopolymer layer, and this

alignment broadens the interface between the two homopolymers. The more s-BCP at the

interface, the more the interface is broadened. It is also evident that the lower MW s-BCP is

more effective in broadening the interface at similar interlayer thicknesses (mass amount). For a

given thickness, the number of low MW s-BCP molecules at the interface is three times that of

the high MW s-BCPs. The higher molar concentration of low MW s-BCPs resulted in more

diffusive interfaces, as observed.

By using PS instead of dPS as homopolymer, the SLD of the PS layer is markedly

changed, becoming comparable in magnitude to the P2VP layer. With the core block of the s-

BCP deuterated, the spatial distribution of the core block provides a contrast to isolate the

location and distribution of the core block at the interface. The NR profile of PS $\|$ (dS-*b*-V)$_4$ $\|$

P2VP trilayers are shown in **Figure 1c,** where the thickness of the (dS-b-V)$_4$ was varied. As

expected, the critical angle for these trilayers has shifted to smaller q, due to the reduced

scattering length density of the top layer of hydrogenated PS. Kiessig fringes are evident in the

NR profile arising predominantly from the thickness of the top PS layer (**Figure 1c**). Using the

known thicknesses of the individual layers, the SLD profiles shown in **Figure S7** were used to fit

the NR data. Since the distribution of the dPS segments in the s-BCP at the interface is expected

to be asymmetric, sharper towards the interface and more diffuse into the PS layer, two Gaussian

functions were merged together to generate the SLD profile. The SLD profile (**Figure 1d**) shows

that the dPS interlayer is consistent with ellipsometry and interferometry measurements of s-BCP

layer thickness. The diffuseness of the "interface" between the dPS block and PS homopolymer

increases significantly with increasing thickness of the (dS-b-V)$_4$ layer for both low and high

MW. In contrast, the width of the interface between the dPS block and P2VP homopolymer layer

increases only slightly with increasing interlayer thickness for thicknesses up to L/2, where L/2

is the single layer period of the s-BCP in the bulk (**Figure S2**).[27] Up to L/2, the s-BCP can form

a monolayer at the interface, while for thicknesses > L/2, there is excess of s-BCP that can be

accommodated at the interface. There are two possible fates of the excess s-BCPs at

equilibrium. Either the excess s-BCP is dissolved in the homopolymer as micelles or s-BCPs

form multilayers at the interface. A dye-labeled 4-arm s-BCPs ((fS36-b-V18)$_4$) were synthesized

by copolymerizing tetramethylrhodamine-5-maleimide with the PS blocks. Since the

copolymerization between styrene and maleimide derivatives is favoring a strong cross

propagation, and polymerization amount of maleimide fluorescent dye is low, the fluorescent dye

is only placed near the core center (arm junction).[32, 33] Therefore, ~15 nm fluorescent interlayer

was directly placed between a PS beam (~3 mm thick) and a P2VP beam (~2 mm thick), and was

annealed to equilibrate. After separating two sheets, the fluorescently labeled s-BCP was found to have diffused into the P2VP (**Figures 2a** and **b**), while the interface between the PS beam remained sharp (**Figure S10**), indicating that the excess s-BCP likely diffused into the P2VP as monomolecular micelles, which is consistent with the SCFT results where the critical micelle concentration (CMC) for s-BCPs in P2VP matrix is infinitely low (**Figure S11**). This result is supported by the absence of interferences at 0.066 Å^{-1}, and 0.027 Å^{-1}, as well as the higher order interference peak of PS ‖ (dS-*b*-V)$_4$ ‖ P2VP for low MW and high MW star BCPs, respectively, which should be present in the reflectivity profile if multilayers formed at interface (**Figure S12**). This was further confirmed by the absence of out-of-plane peak from grazing-incidence small angle neutron scattering (GISANS) on the same sample (**Figure S13**).[34] The indiscernible in-plane peaks also suggested that the intermolecular spacing between these s-BCPs at interface is poorly defined, which potentially originate from the inherent softness of these s-BCPs. This hypothesis is supported by the presence of prominent in-plane peak when same s-BCPs become much more rigid when P2VP blocks carries charge at the fluids interface.[23]
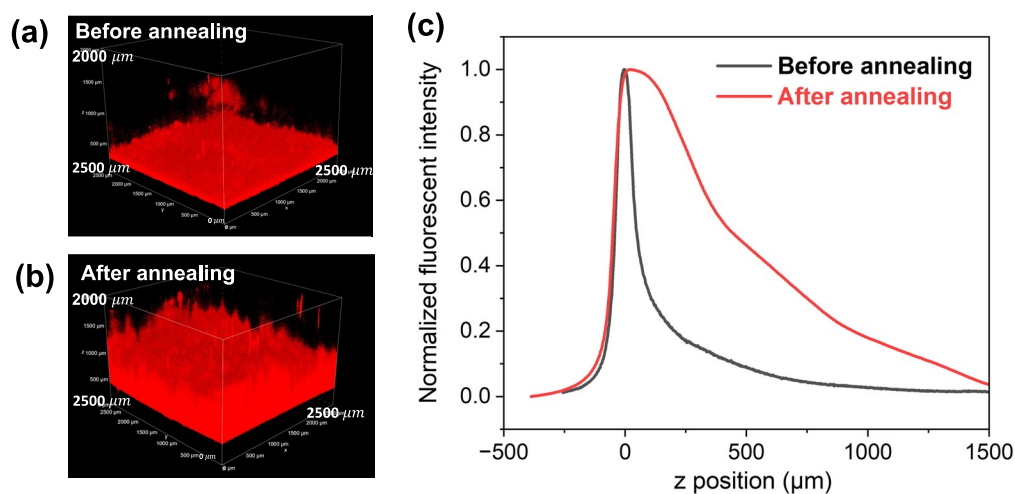
Figure 2. A trilayer containing excessive (15 nm thickness) fluorescent star block copolymers (s-BCPs) at homopolymer interface and the confocal laser scanning fluorescent microscopy images of P2VP beam for **(a)** before annealing and **(b)** after annealing and **(c)** corresponding fluorescent intensity as function of z height. The fluorescent s-BCPs is placed at z=0 on the P2VP beam. The P2VP layer is in positive z position.

Segmental density distribution as revealed by neutron reflectivity (NR)

Detailed segmental density distributions are critical in understanding the conformation of the s-BCPs at the homopolymer interface. PS ‖ (dS-*b*-V)$_4$ ‖ P2VP trilayers afford the distribution of segments of the PS homopolymer, PS block of the s-BCP, and the P2VP segments of the s-BCP along with those of the P2VP homopolymers. As shown in **Figure 3** and **Figure S14**, the dPS block is located near the PS homopolymer side of the interface for both the low and high MW, as expected. The surface excess (Γ) of the dPS block can be obtained by integrating dPS block over z height ($\Gamma = \int_{-\infty}^{\infty} \Phi_{dPS\,s-BCPs}\,d_z$), where $\Phi_{dPS\,s-BCPs}$ is the volume fraction of dPS blocks for s-BCPs, and z is the height. The calculated Γ is consistent with the independent interlayer thickness measurements as summarized in **Table 2**. With increasing interlayer thickness, the maximum volume fraction of dPS block ($\Phi_{maximum}$) increased for both the low MW and high MW s-BCPs, with the high MW s-BCP having a higher $\Phi_{maximum}$ than low MW s-BCP at a similar interlayer thickness and reaches saturation at 0.71 at medium interlayer thickness (~8 nm). Similarly, the full-width half maximum (FWHM) of the segment density distribution of the dPS block of the s-BCP increased with increasing interlayer thickness, with low MW s-BCP having a

16

larger FWHM than high MW s-BCP. These result show that low MW s-BCP creates more broaden interface at similar interlayer thickness, which is consistent with interfacial width results.
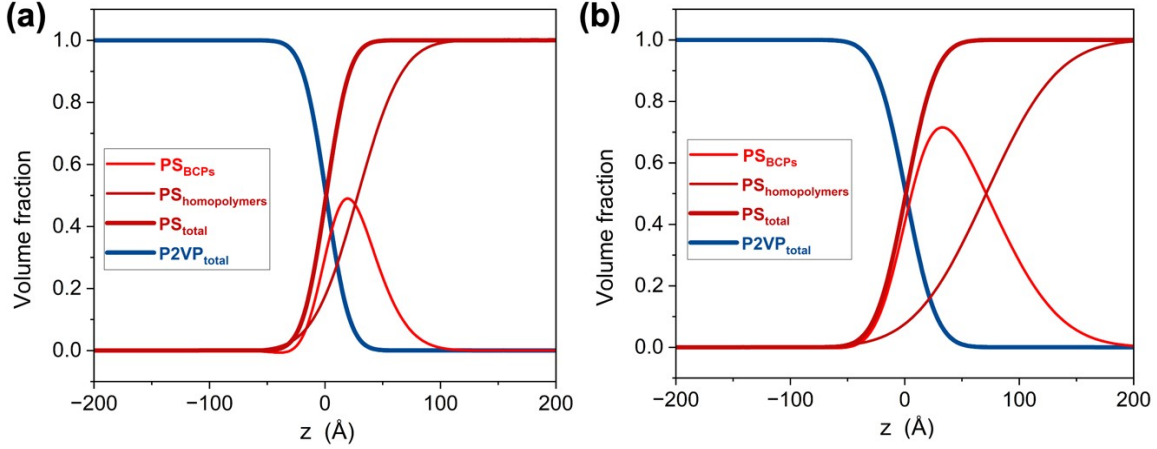
Figure 3. Representative segmental density distribution of s-BCPs at homopolymer interface solved from the neutron reflectivity (NR) with PS ‖ (dS-*b*-V)₄ ‖ P2VP contrast. The volume of different segments is plotted as a function of z, the distance from the homopolymer interface. High MW s-BCPs with interlayer thickness **(a)** 3.4 nm and **(b)** 14.9 nm. Z is shifted to align the interface at z=0.

Interfacial area of the PS block per s-BCP molecule or per arm ($A_{per\,star}$ or $A_{per\,arm}$) can be

calculated by $A_{per\,star} = \dfrac{M_{s-BCPs}/\rho_{s-BCPs}}{N_A \displaystyle\int_{-\infty}^{\infty} \Phi_{PS\,s-BCPs}\,d_z}$, and $A_{per\,arm} = \dfrac{A_{per\,star}}{4}$, where $M_{PS\,s-BCPs}$ is MW of s-

BCPs, ρ_{s-BCPs} is the density of s-BCPs (taken as 1.10 g/cm³), and N_A is Avogadro's number.

$A_{per\,star}$ and $A_{per\,arm}$ was found to decrease with increasing interlayer thickness. As shown in

17

Scheme 2a, with increasing packing density of the s-BCPs at the interface, the arms must assume a more perpendicular orientation to accommodate more BCPs per unit area. The larger interfacial width with increasing s-BCP concentration would broaden the segment density distribution of s-BCPs normal to the interface. By adding $\Phi_{PS\,s-BCPs}$ and $\Phi_{PS\,homopolymers}$, one gets $\Phi_{PS\,total}$ segments. By plotting this with $\Phi_{P2VP\,total}$, a direct comparison to the results from the dPS || (dS-*b*-V)$_4$ || P2VP trilayer can be made (**Figure S15**). The results show that at low and medium interlayer thickness, the total segments distribution is comparable for both low and high MW s-BCPS. However, at the highest interlayer thickness, the interfacial widths are significantly broader for dPS || (dS-*b*-V)$_4$ || P2VP than PS || (dS-*b*-V)$_4$ || P2VP contrast, which can be attributed to the dissolution of unimolecular micelles of (dS-*b*-V)$_4$ in P2VP along with an increase of interfacial width. Alternatively, if the position of each layer is unknown, we can also obtain the segmental density distributions by solving the two SLD profiles of PS || (dS-*b*-V)$_4$ || P2VP and dPS || (S-*b*-V)$_4$ || P2VP simultaneously (**Figure S16** and **Table S1**).[25] The unusual distribution of segments (above 1 or below 0) at some locations could arise from slight difference in the interlayer thicknesses in the two cases. The differences in the MWs and volume fractions of the D-labeled s-BCPs and H-labeled s-BCPs can also contribute to the discrepancy.

Table 2. Summarized interfacial assembly of PS blocks for s-BCPs at homopolymer interface as revealed by neutron reflectivity measurement with PS || (dS-*b*-V)$_4$ || P2VP contrast.

Samples	$\Phi_{maximum}{}^{a}$	FWHM^{b} (Å)	$\Box^{c}$ (Å)	$\Box_{per\,star}{}^{d}$ (Å^2)	$\Box_{per\,arm}{}^{e}$ (Å^2)
Low MW 3.0 nm	0.43	53	23	986	246
Low MW 7.6 nm	0.58	67	42	540	135
Low MW 13.9 nm	0.61	112	73	310	78
High MW 3.4 nm	0.49	52	28	2508	627

High MW 8.0 nm	0.71	64	49	1433	358
High MW 14.6 nm	0.71	92	70	1003	251

[a] maximum volume fractions (Φ) of dPS block for s-BCP. [b] full-width half maximum (FWHM) of dPS block for s-BCP. [c]

surface excess (Γ) calculated by $\Gamma = \int_{-\infty}^{\infty} \Phi_{dPS\,s-BCPs} d_z$. [d] interfacial area per star BCPs molecule ($A_{per\,star}$),

calculated by $A_{per\,star} = \dfrac{M_{dPS\,s-BCPs} / \rho_{dPS-BCPs}}{N_A \int_{-\infty}^{\infty} \Phi_{dPS\,s-BCPs} d_z}$. [e] interfacial area per arms of star BCPs molecules (

$A_{per\,arm}$), calculated by $A_{per\,arm} = \dfrac{A_{per\,star}}{n_{arm\,number}}$

## Block and junction point density distribution solved from self-consistent field theory (SCFT)

SCFT calculations were also used to calculate the segment (block) density distributions of the s-BCPs at the homopolymer interface. The volume-based degree of polymerization for the PS block and P2VP block of s-BCPs and PS, P2VP homopolymer are modeled from the experimental system. Due to the presence of bimolecular s-BCPs, as indicated by SEC (**Figure S3**), it is important to compare the conformation of the s-BCP and the corresponding bimolecular s-BCP (**Figure 4a**). As shown in **Figures 4b** and **Figure S17,** the segment density distributions of the two are indistinguishable for both low MW and high MW s-BCPs, indicating the coupling of the arm ends has a neglectable effect on their interfacial conformation. Therefore, we used only the single 4-arm s-BCP in the SCFT calculations.
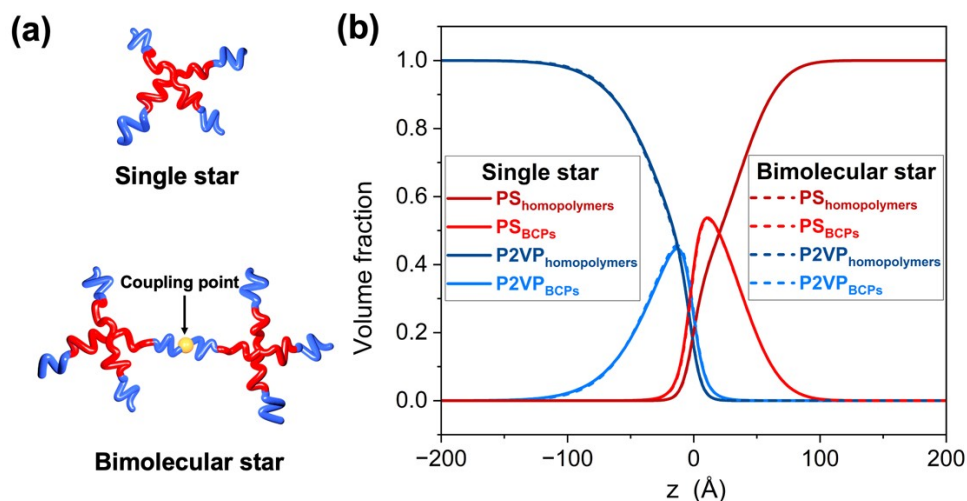
Figure 4. Comparison of interfacial conformation between single star block copolymer (s-BCP) and bimolecular s-BCPs with SCFT. **(a)** Structure of single star BCPs and bimolecular star BCPs. **(b)** SCFT results of 5.0 nm high MW star BCPs between 80 nm PS homopolymer and 80 nm P2VP homopolymer, with the volume fraction, plotted as a function of the distance from the homopolymer interface (z). z is shifted to align the interface at z=0.

Figure 5 shows that the SCFT segment density distributions are consistent with the NR results. Consequently, using SCFT to map the real s-BCP interfacial conformation is reasonable. Further increasing the interlayer thickness of the low MW s-BCP well above L/2 yield a multilayer of s-BCPs for low MW from the SCFT calculations (**Figure S18**), since the SCFT calculations eliminate the possibility of forming unimolecular micelles in the P2VP phase. The detailed block and homopolymer segment distribution, as determined by SCFT, are summarized in **Table 3** and **Table S2-S3**. From the SCFT calculations we can also determine the spatial distribution of the arm junction points, the block junction points, and the arm ends (**Figure 6a**), which offer crucial insights into investigating architecture-governed interfacial conformation. As shown in **Figure S19**, the interface between total segments of PS and P2VP is sharper for high

MW than low MW at same interlayer thickness, which agrees with the NR results. The PS and

P2VP blocks have broader segment density distributions at the interface for high MW s-BCPs

and are more concentrated for low MW s-BCPs with a 5 nm interlayer thickness, which is

quantitatively described by larger $\Phi_{\text{P2VP/PS}}$ and smaller FWHM$_{\text{P2VP/PS}}$ for low MW s-BCP, as

summarized in **Table S2** and **Table S3**. This is in contrast with the NR results, where low MW

resulted in a larger segment density distribution of the PS blocks. Since the low MW s-BCP has a

larger measured interfacial width, capillary waves at the interface,[30] could easily broaden the

interfacial width determined experimentally, because the SCFT calculations make use of a

planar, flat interface. As shown in **Figure 6b-c**, the arm junctions of the low MW s-BCP are

most concentrated near the interface, while the block junctions are most concentrated for the

high MW s-BCP. The former is counterintuitive, since the block junction that is the junction

between the two different blocks should have the narrowest distribution. We note that the low

MW s-BCP has roughly a factor of three higher packing density than high MW s-BCP for the

same interlayer thickness. The packing density is given by $\dfrac{\rho * h * A/M}{A} = \dfrac{\rho * h}{M}$, where ρ is the

density of s-BCPs (assumed to be 1.10 g/cm^3), h is interlayer thickness, A is interfacial area and

M is the MW of s-BCPs. If we assume that an interlayer thickness of L/2 saturates the interface

with a monolayer of s-BCPs (**Figure S20**), interlayer thicknesses much lower than this yields

loosely packed assemblies and slightly higher overpacks the interface, as discussed earlier.
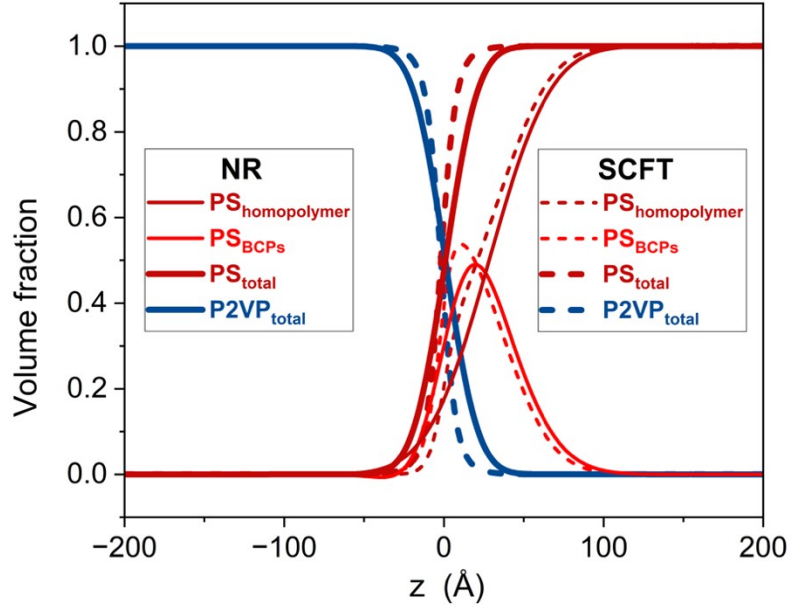
Figure 5. Comparison of segmental density distribution between neutron reflectivity (NR) and self-consistent field theory (SCFT) with similar PS block surface excess. High MW of s-BCPs is used as an example. The volume fraction is plotted as a function of the distance from the homopolymer interface (z).

Table 3. Summarized block distributions of star block copolymers and linear block copolymers at homopolymer interface as revealed by self-consistent field theory.

Architecture [a]	MW [b]	Packing density (*10^-7 mol/m²) [c]	Φ_{P2VP} [d]	FWHM$_{P2VP}$ (Å) [e]	Φ_{PS} [f]	FWHM$_{PS}$ (Å) [g]
Star BCPs	Low	0.5	0.20	31	0.28	29
Linear BCPs	Low	0.5	0.16	31	0.19	32
Star BCPs	Low	1.5	0.49	37	0.65	37
Linear BCPs	Low	1.5	0.37	35	0.44	37
Star BCPs	High	0.5	0.45	45	0.54	46

|						
Linear BCPs	High	0.5	0.45	45	0.48	48
Star BCPs	High	1.5	0.92	67	0.96	77
Linear BCPs	High	1.5	0.92	67	0.95	76

[a] linear BCPs is set as same as star BCP's arm. [b] Low MW: each arm has a repeating unit of PS block and P2VP block 48 and 40, respectively. High MW: each arm has a repeating unit of PS block and P2VP block 129 and 149, respectively. [c] Packing density

is calculated as $\dfrac{\rho * h}{M}$, where ρ is the density of s-BCPs and taken as 1.10 g/cm^3, h is s-BCPs interlayer thickness, M is the MW

of s-BCPs. When packing density = $0.5*10^{-7}$ mol/m^2, it is loosely packed (h is much smaller than L/2); when packing density = $1.5*10^{-7}$ mol/m^2, it is overpacked (h is slightly larger than L/2). [d] Maximum of P2VP block volume density distribution. [e] Full-width half maximum of P2VP block volume density distribution. [f] Maximum of PS block volume density distribution. [g] Full-width half maximum of PS block volume density distribution.

To eliminate the effect of packing density on junction point distribution of s-BCPs conformation, we calculated another two interlayer thicknesses so that both low MW and high MW BCPs have loosely packed and over packed thicknesses. At the same packing density, the two MW s-BCPs have similar total segment distributions (**Figure S21**), indicating that the packing density (molar concentration) is the main reason for different interfacial widths rather than MW. As summarized in **Table 3**, PS and P2VP blocks of high MW s-BCPs always have higher values of Φ and FWHM at the same packing density. It is also noted in **Table 4** that the distribution of arm junctions of the low MW s-BCP is always the most concentrated, regardless of packing density, yet the distributions of block junctions is always the sharpest for high MW s-BCP. These results infer that the arm junctions of low MW s-BCPs are more immobile than the block junctions, that may arise from the arm junction being more strongly anchored to the interface in a very limited z-position range. In contrast, the high MW arms have sufficient

conformational entropy to accommodate the penetration of homopolymer, thereby giving a more mobile arm junction (**Scheme 2b**).
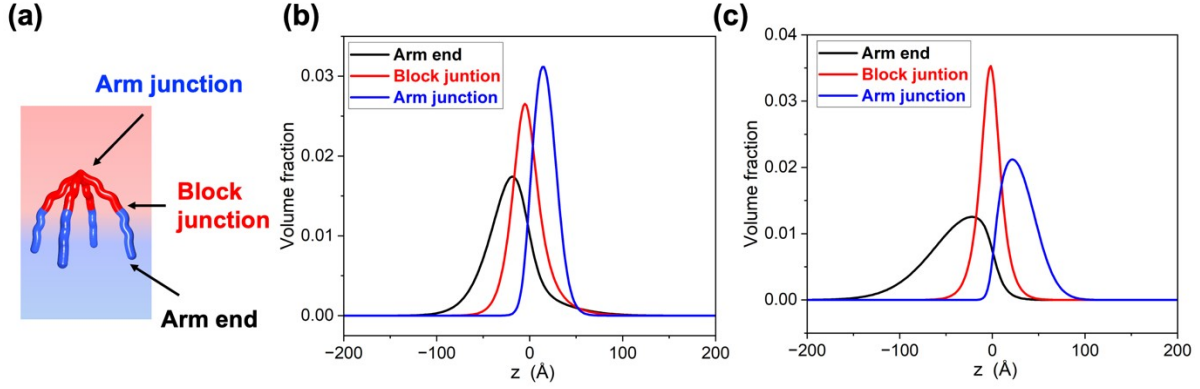
Figure 6. Probing star block copolymers (s-BCPs) interfacial conformation by self-consistent field theory (SCFT). **(a)** Scheme of junction points in s-BCPs. Junction point density distribution of **(b)** low MW and **(c)** high MW with 5 nm interlayer thickness.

Table 4. Summarized junction points distributions of star block copolymers at homopolymer interface as revealed by self-consistent field theory.

Architecture [a]	MW [b]	Packing density ($*10^{-7}$ mol/m^2) [c]	$\Phi_{arm\ end}$ [d]	FWHM arm end (Å) [e]	$\Phi_{block\ junction}$ [f]	FWHM block junction (Å) [g]	$\Phi_{arm\ junction}$ [h]	FWHM$_{arm\ junction}$ (Å) [i]	$d_{arm\ end}$ (Å) [j]	$d_{arm\ junction}$ (Å) [k]
Star BCPs	Low	0.5	0.020	45	0.034	25	0.039	24	17	15
Linear BCPs	Low	0.5	0.018	45	0.030	25	0.017	47	18	21
Star BCPs	Low	1.5	0.017	48	0.027	31	0.031	30	18	18
Linear BCPs	Low	1.5	0.015	47	0.025	29	0.016	50	19	22
Star BCPs	High	0.5	0.01	74	0.03	24	0.02	46	39	32

			3		5		1			
Linear BCPs	High	0.5	0.013	74	0.035	24	0.012	80	40	44
Star BCPs	High	1.5	0.012	80	0.031	27	0.018	53	52	57
Linear BCPs	High	1.5	0.012	80	0.031	27	0.011	88	52	59

[a] linear BCPs is set as same as star BCP's arm. . [b] Low MW: each arm has a repeating unit of PS block and P2VP block 48 and 40, respectively. High MW: each arm has a repeating unit of PS block and P2VP block 129 and 149, respectively. [c] Packing density is calculated as $\dfrac{\rho * h}{M}$, where ρ is the density of s-BCPs and taken as 1.10 g/cm^3, h is s-BCP interlayer thickness, M is the MW of s-BCPs. When packing density = $0.5*10^{-7}$ mol/m^2, it is loosely packed (h is much smaller than L/2); when packing density = $1.5*10^{-7}$ mol/m^2, it is overpacked (h is slightly larger than L/2). [d] Maximum of arm end volume density distribution. [e] Full-width half maximum of arm end volume density distribution. [f] Maximum of block junction volume density distribution. [g] Full-width half maximum of block junction volume density distribution. [h] Maximum of arm junction volume density distribution. [i] Full-width half maximum of arm junction volume density distribution. [j] Arm end average distance is calculated by

$$d_{arm\,end}=\frac{\int_{-\infty}^{\infty} z\, d\Phi_{block\,junction}}{\int_{-\infty}^{\infty} d\Phi_{block\,junction}}-\frac{\int_{-\infty}^{\infty} z\, d\Phi_{arm\,end}}{\int_{-\infty}^{\infty}\Phi_{arm\,end}}.$$

[k] Arm junction average distance is calculated by

$$d_{arm\,junction}=\frac{\int_{-\infty}^{\infty} z\, d\Phi_{arm\,junction}}{\int_{-\infty}^{\infty}\Phi_{arm\,junction}}-\frac{\int_{-\infty}^{\infty} z\, d\Phi_{block\,junction}}{\int_{-\infty}^{\infty} d\Phi_{block\,junction}}.$$

Architecture-directed interfacial conformation

The different distributions of block and junction points for the s-BCPs arise from the star architecture, where the core bock (PS) is attached, on one end, to the central junction point (arm junction), and the other end of the block is attached to the corona block (P2VP). The corona block (P2VP), in contrast, can move in a freer manner. Linear BCPs that are chemically and compositionally the same as the arms of the s-BCPs arm are only restricted at the junction point, thereby, a symmetric distribution of the block segments on opposite sides of the interface would be expected. Comparing the distributions of the block and junction points (including arm junction, block junction and arm ends) between two architectures would further demonstrate the influence of the star architecture on interfacial conformation. For the case with an excess amount of low MW s-BCPs in comparison to its linear counterpart, the s-BCP showed a higher amount of segregation to the interface, due to the solubility of the low MW linear BCPs in the homopolymer phases (**Figure S22b**). However, for the high MW case, the distribution of the P2VP blocks at the interface are essentially the same for the linear and star cases while, for the PS block, the s-BCP showed a slightly higher concentration at the interface (**Figure 7a**). Even with the differences in block distributions for the two architectures, we found the total segments distribution and interfacial width between total PS and P2VP segments are mainly determined by the packing density rather than architecture (**Figure 7b** and **Figure S22c**). It is also not surprising to observe that low MW linear BCPs, unlike the star architectures, have the higher concentration of block junctions at the interface (**Figure S22c**). The high MW linear and star copolymers showed similar distributions of arm end and block junctions. The arm junctions of s-BCPs are more concentrated at the interface than those of the linear BCPs, due to the restrictions on the architecture (**Figure 7c**). When the packing density is decreased, the difference between

star BCPs and linear BCPs on interfacial conformation remains similar (**Figure S23** and **Table S2-S5**).
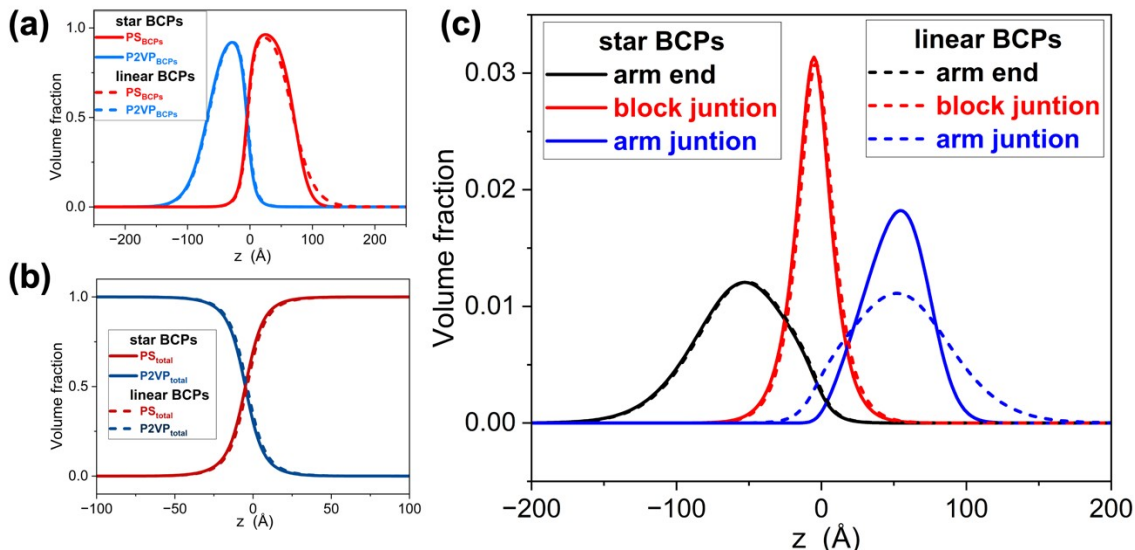
Figure 7. Self-consistent field theory (SCFT) results of **(a)** block distribution, **(b)** total segments distribution and **(c)** junction point distribution between high MW of star BCPs and linear BCPs at packing density=$1.5*10^{-7}$ mol/m^2(over packed). Linear BCP has same chemical and MW composition as arm of star BCPs. The interface between P2VP and PS is set as 0 position.

In addition to the junction density distribution, the physical intramolecular distance between junctions (including the average arm end distance $d_{arm\,end}$ and average arm junction distance $d_{arm\,junction}$) was also calculated using

$$d_{arm\,end/junction} = \dfrac{\displaystyle\int_{-\infty}^{\infty} z\,d\Phi_{arm\,end/junction}}{\displaystyle\int_{-\infty}^{\infty} d\Phi_{arm\,end/junction}} - \dfrac{\displaystyle\int_{-\infty}^{\infty} z\,d\Phi_{block\,junctiom}}{\displaystyle\int_{-\infty}^{\infty} d\Phi_{block\,junctiom}} \vee \dot{c},$$ as summarized in **Table 4**. It was

observed that both $d_{arm\,end}$ and $d_{arm\,junction}$ increased for larger interlayer thickness, suggesting s-

BCPs were stretched across the interface to accommodate the higher packing density, which is

consistent with the NR results showed that the PS block interfacial area decreased at higher

packing densities. It was also found that the ratio of $d_{arm\,junction}$ to $d_{arm\,end}$ distance depends on

packing density, showing ratio increase as the packing density increased, which is also MW-

dependent. Specifically, $d_{arm\,junction}$ is always smaller than $d_{arm\,end}$ for both low MW and high MW

s-BCPs at low packing densities (loosely packed). However, at high packing density, $d_{arm\,junction}$

become equal to $d_{arm\,end}$ for low MW and even greater than $d_{arm\,end}$ for high MWs. With the

results that linear BCPs always have $d_{arm\,junction}$ greater than $d_{arm\,end}$ regardless of the MW or

packing density, the trend observed for s-BCPs can only arise from the architecture effect.

To elucidate the origin of the effect, we simulated linear BCPs at two packing densities,

where the chemical composition of linear BCPs is the same as the s-BCPs arm. Since linear

BCPs have, on average, an orientation normal to the interface and both blocks are equally wetted

by homopolymer, it can be used as a reference for probing the interfacial conformation of the s-

BCPs. We define a parameter, $\Box$, that is relative difference between $d_{arm\,end}$ and $d_{arm\,junction}$ of

linear BCPs and star BCPs, where $\Delta_{arm\,junction} = \dfrac{d_{star\,arm\,junction}}{d_{linear\,arm\,junction}} - 1$, and similarly for $\Delta_{arm\,end}$ (**Figure**

8a). When $\Box = 0$, the arm junction/end of s-BCPs are same stretched to the same degree as linear

BCPs, thus the conformation is not affected by the architecture; when $\Box < 0$, the arm junction/end

of star BCPs is closer to interface than linear BCPs; when ☐ > 0, the arm junction/end of star

BCPs is more stretched away from interface than linear BCPs. As seen in **Figure 8b**, for both

low MW and high MW copolymers, ☐ <0 for low packing densities and increases at higher

packing densities. For high MW, ☐ is closer to 0 than for low MW and reach 0 at medium

packing density. Moreover, the ☐ of arm junction is more negative than that of the arm end,

indicating architecture causes the arm junction to be closer to the interface than the arm end. In

terms of MW, the arm junction for high MW is closer to 0 than low MW, but is always below 0,

even at high packing densities (**Figure 8d**). These results show that both low MW and high MW

s-BCPs are more compressed in the z-direction than the corresponding linear BCPs at low

packing densities, but for higher MW s-BCPs, there is more configurational entropy, so that it is

less impacted from the architectures (**Scheme 2c**). At higher packing densities, the corona blocks

of high MW s-BCPs behave the same configurationally as the linear BCPs, since they are less

confined by arm junction than core blocks.

From the above arguments, one can also approximate the inclination angle, ξ, for the arm

end and arm junction using $\xi \dot{\iota} \arcsin \left(\dfrac{d_{star\,arm\,junction/end}}{d_{linear\,arm\,junction/end}} \right)$ by assuming linear BCPs and star BCPs

have the same "arm" length, which is the value that defines how the arm aligns from normal

orientation with respect to the interface (**Figure 8a**). **Figure 8c** shows both arm ends of low MW

and high MW are tilted at low packing densities. With increasing packing density, an orientation

more normal to interface is found, and at even higher packing densities, a normal orientation is

found for high MW. **Figure 8e** shows a higher inclination angle of the arm junction than the arm

end, with low MW s-BCPs having a larger inclination angle than high MW. This result further

demonstrates that at low packing density, low and high MW of s-BCPs extend their arms parallel to the interface to maximize interface coverage. Since high MW s-BCPs have a larger configurational entropy, it is easier to overcome the confinements at the arm junction, yielding a more normal orientation. At packing densities near saturation, an orientation more normal at the interface is found for both arm end and arm junctions, making interfacial conformation of low MW and high MW s-BCPs more akin to linear BCPs, whereas the arm junctions still differ.
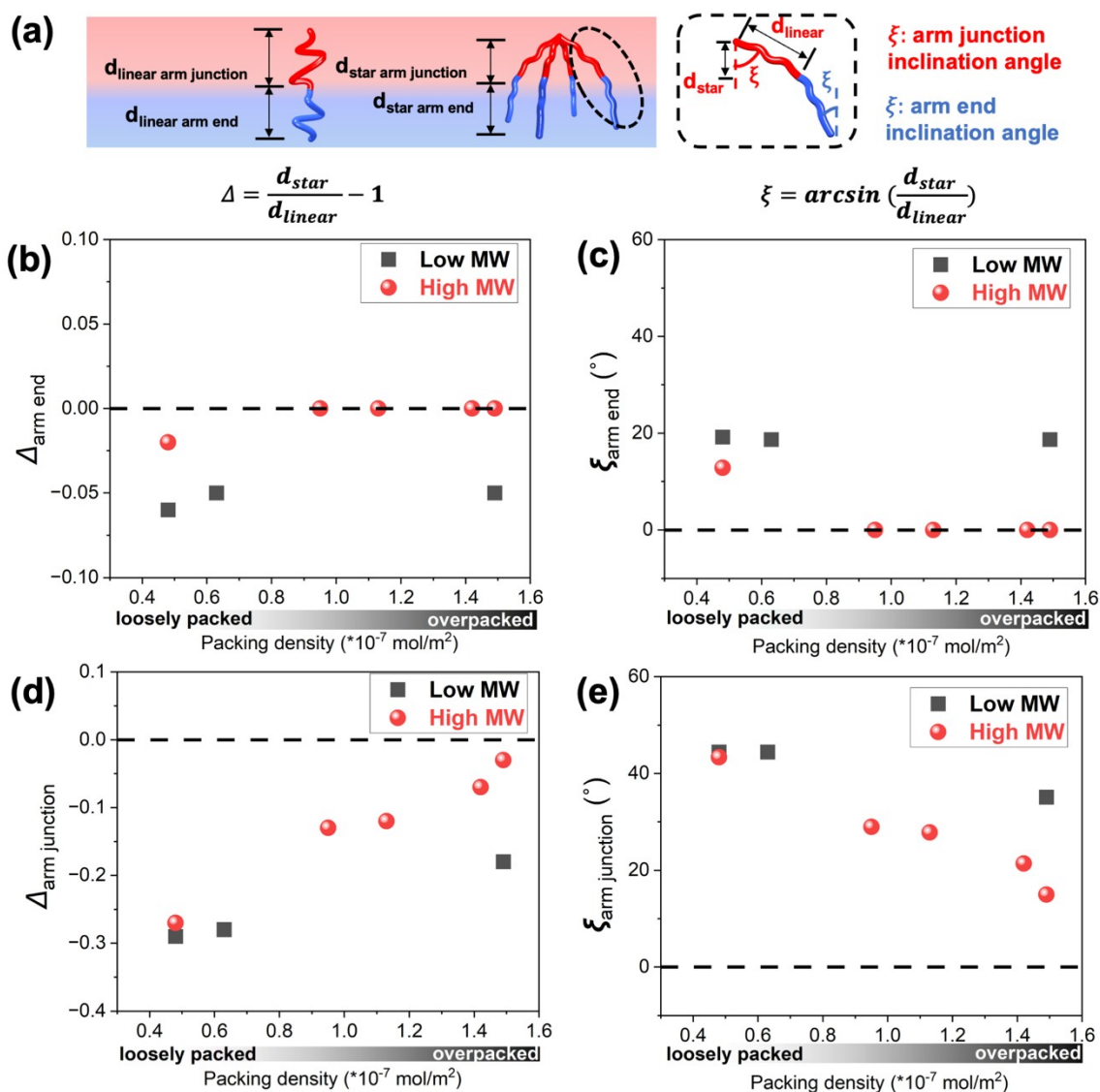
Figure 8. Molecular weight and packing density-dependent of star block copolymers (s-BCPs) interfacial conformation normalized by linear BCPs. **(a)** Scheme of calculation. Shift degree($\square$) of **(b)** arm end and **(d)** arm junction as a function of packaging density. The inclination angle (ξ) of **(c)** arm end and **(e)** arm junction as a function of packaging density. The dashed line in the figure indicates the same conformation as linear BCPs.

Compatibilization efficiency
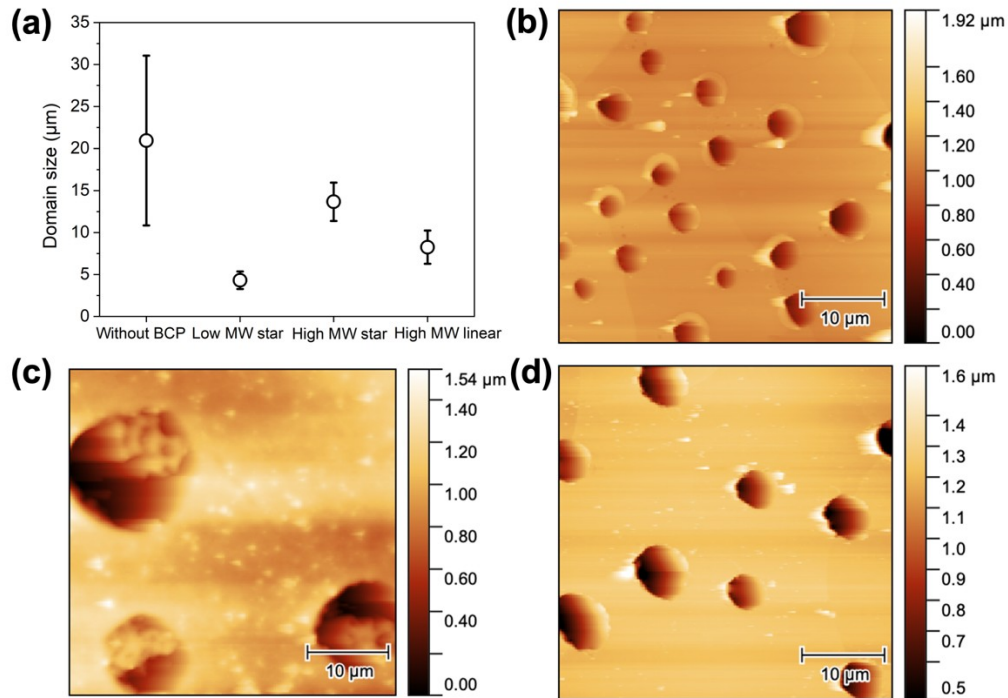
Figure 9. Phase behaviors of PS/P2VP blend film upon addition of BCPs. **(a)** domain size, measured by optical microscopy. Atomic force microscopy (AFM) results of blend phase

behaviors for **(b)** low MW s-BCPs, **(c)** high MW s-BCPs and **(d)** high MW linear BCPs. The proportion of PS to P2VP is 70 wt% to 30 wt%. 10 wt% BCPs is added as compatibilizer. P2VP domains were washed by ethanol after phase separation reaching equilibrium.

To test the compatibilization efficiency of s-BCPs, we investigated the phase behaviors of the thin film of polymer blends contained PS and P2VP homopolymer. Due to the phase separation between two immiscible polymers, blends will yield large particles (homopolymer with lower volume fraction) distributed in surrounding matrix (homopolymer with higher volume fraction) to minimize the interfacial area for lowering interfacial energy. The high interfacial energy between immiscible polymers is responsible for the poor mechanical properties of recycled plastic composite, since the weak adhesion between particle and surrounding matrix will limit stress being transferred between domains and lead interfacial failure occurred.[35] The introduction of s-BCPs additives, as we showed previously, can efficiently increase the interfacial width between two homopolymers, therefor lowering the interfacial energy and reducing the domain sizes. It may also improve the adhesion between two homopolymers due to enhanced interdiffusion and increased physical entanglement between two homopolymers.[36]

We prepared the polymer blends film with P2VP domain spread across PS matrix by first dissolving PS and P2VP homopolymer as well as BCPs in common solvent. After drop casting the solution onto a wafer followed by air drying, we thermally annealed the film to reach equilibrium of phase separation and interfacial assembly of BCPs. The P2VP domain was further washed by ethanol to give contrast. As shown in **Figure S26** and **Figure 9a**, we found all BCP additives can efficiently reduce the domain size compared to the blend absent BCPs. At 10 wt.% concentration, low MW s-BCPs yield smaller domain sizes in comparison to high MW s-BCPs,

as a result of the lower interfacial energy, which is consistent with interfacial width findings.

Since the molecular weight of the high MW s-BCPs is ~3 times that of the low MW s-BCPs, we

prepared low MW s-BCP with 3.3 wt.% to reach same molar concentration as high MW s-BCPs.

It showed low MW s-BCPs have similar domain sizes at two mass concentration, indicating

interfacial assembly of s-BCPs reached saturation in both cases (**Figure S26** and **S27**). We also

found high MW linear BCPs have smaller domain sizes compared by high MW s-BCPs.

However, upon careful examination of the morphology of blend with atomic force microscopy

(AFM), we found low MW s-BCPs (**Figure 9b**) and high MW linear BCPs (**Figure 9d**) give

regular, spherical domain shape, as expected. In contrast, high MW s-BCPs yield complex

domain shapes, arising from the jamming of the interfacial assemblies that arrested the phase

separation between PS and P2VP homopolymers (**Figure 9c**). This indicates that high MW s-

BCPs have significantly higher interfacial binding energy in comparison to low MW s-BCPs and

high MW linear BCPs. Only s-BCPs with high binding energy can trap the morphology during

phase separation, otherwise they will be ejected out from interface as the system decreases

interfacial area.[37] The high binding energy can also increase the adhesion strength between two

homopolymers, and, therefore, improve the compatibilization efficiency.

The adhesion strength (critical energy release rate Gc) between PS and P2VP with the s-

BCPs at the interface was measured by inserting a razor blade between homopolymers beams

using the asymmetric double cantilever beam (ADCB) test (**Figure 10a**).[8, 24] The energy release

rate can be calculated by $G_C = \dfrac{3 \Delta_{razor}^2 E_1 h_1^3 E_2 h_2^3}{8 \alpha^4}$ ¿, where $C_1 = 1 + 0.64 \dfrac{h_1}{\alpha}$, $C_2 = 1 + 0.64 \dfrac{h_2}{\alpha}$,

subscript 1 and 2 stands for PS and P2VP, respectively. The E is Young's modulus, h is the

thickness of the beam, a is the crack length (distance from the razor blade to the crack tip, which is measured after insertion of the razor blade overnight), and Δ_{razor} is the thickness of the razor blade. [24] Linear BCPs with arm lengths similar to the arms of the s-BCPs were used for comparison. Fluorescently labeled s-BCPs were used to track the s-BCP distribution after the separation of two beams. Fluorescent labelling is only introduced in the core block center, making fluorescence specific to PS block. Fluorescence was observed on both the PS and P2VP beam (**Figure 2b** and **Figure S10**) post separation of the two beams, suggesting a chain pull-out mechanism. Compared to chain scission mechanism in which PS block would be remained only in PS beam side, the chain pull-out mechanism yield PS blocks trapped on both beam side (**Figure S28**). Additionally, both beam surfaces remained smooth after separation, suggesting an adhesive failure mechanism, which is commonly observed with chain pull-out. As **Figure 10b** shows, Gc increases and plateaus for all BCP cases, with s-BCPs having much larger Gc's than their linear counterparts, even the low MW s-BCPs had slightly larger Gc's than high MW linear BCPs. Since a single s-BCPs molecule has four arms (some may have eight arms due to the presence of bimolecular stars) at the interface, compared to a single "arm" for linear BCPs, the binding energy of a single s-BCP is significantly strengthened, as we showed in previous studies. The higher MW copolymers have higher degrees of interaction between blocks with the homopolymers, thus the adhesion is further promoted. We note that Gc of s-BCPs exported here differs from that reported previously for the linear BCP system, but the MW for the linear BCP is at least 10 times higher than that of the arm lengths in this study, which is well beyond the entanglement of MW.[24] This suggests that by increasing the MW of the arms, the adhesion of the s-BCP can be further improved, yielding more efficient stress transfer in blend system. [35]
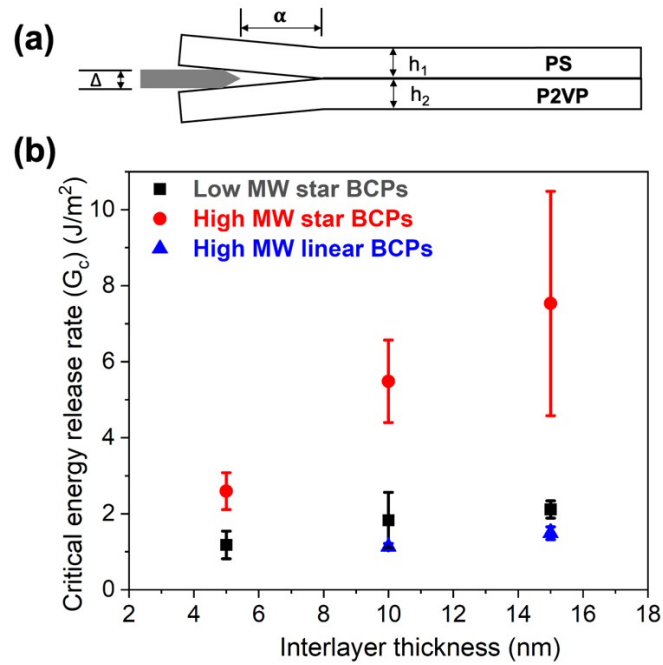
Figure 10. Adhesion behavior of star block copolymers (s-BCPs) and linear BCPs measured by asymmetric double cantilever beam (ADCB) test. **(a)** Scheme of the adhesion measurement. **(b)** Energy release rate (Gc) as a function of interlayer thickness, MW, and BCPs architectures.

(a) Concentration-dependent conformation
(High MW as example)

Loosely packed   **Over packed**
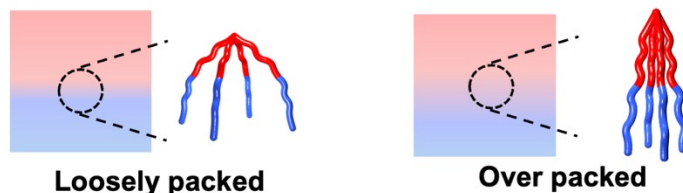
(1) Decreasing interfacial area per star BCP
(2) Decreasing inclination angle of arm end and arm junction
(3) Increasing interfacial width and distribution of star BCPs normal to the interface

(b) MW-dependent conformation
(Same interlayer thickness (loosely packed) as example)

Low MW   **High MW**

(1) Decreasing interfacial width
(2) Arm oriented more normal to interface (less impacted by architecture confinements)
(3) Arm has more conformation entropy to interact with homopolymer

(c) Architecture-dependent conformation
(High MW as example)

Linear BCPs   **4-arm star BCPs**

Loosely packed

Over packed
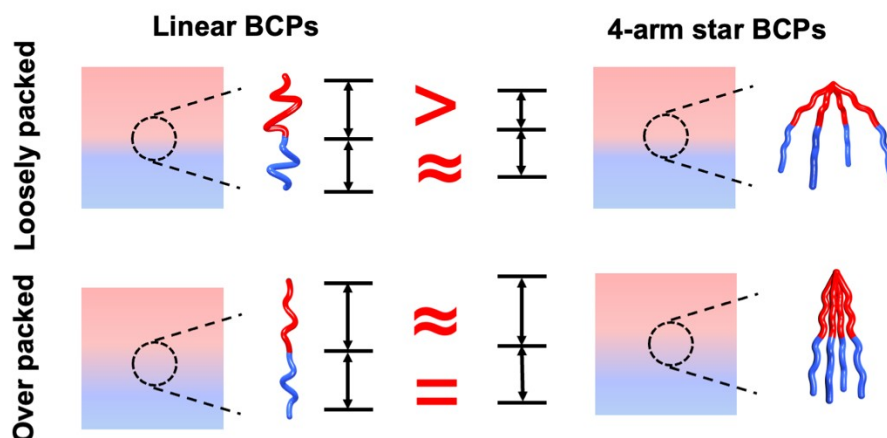
(1) Arm junction is more compressed near the interface than arm end
(2) Arm junction has larger inclination angle than arm end
(3) Increasing packing density, 4-arm star BCPs orient more like linear BCPs

Scheme 2. Schematic illustration of star blocks copolymers (s-BCPs) interfacial configuration between homopolymer interface.

Conclusion

In summary, we first studied the configuration of star block copolymers (s-BCPs) between two homopolymer interfaces by neutron reflectivity (NR) and self-consistent field theory (SCFT) as a function of the packing density, MW, and architecture. Both NR and SCFT results show that s-BCPs can significantly increase the interfacial width between two homopolymer, and increasing the packing density can further broaden the interface. Excess s-BCPs were found to be released from the interface in the form of unimolecular micelles into the corona-miscible phase, rather than constituting multilayers at the interface. The interfacial area occupied by the PS blocks was found to decrease at higher packing densities, indicating s-BCPs compress their in-plane configuration and orient more normal to interface. This concentration-dependent orientation of the s-BCPs was confirmed by the SCFT calculations. SCFT also reveals that core blocks are more concentrated than corona blocks. Furthermore, it is also found the arm junction is more compressed near the interface than arm end. Both parameters show MW dependence. Using linear BCPs as a reference, the inclination angle of the arm junction and arm end for s-BCPs, according to SCFT calculations, decreases at higher packing densities. Increasing MW of s-BCPs can also decrease inclination angle, orienting more like linear BCPs. The interfacial behaviors were further translated into macroscopic compatibilization efficiency. All s-BCP additives can efficiently reduce the domain size compared to pure blend. Low MW s-BCPs can produce smaller domain size due to lower interfacial tension and higher interfacial width, and high MW s-BCPs can arrest the phase separation to give complex domain morphologies due to higher binding energy and jamming of the assemblies at the interface. Adhesion results also show that s-

BCPs are more efficient in promoting adhesion than their linear BCPs counterparts, due to stronger binding energy per single molecule. The result shown here provide a basis for the use of s-BCPs as efficient compatibilizer, and eventually, universal compatibilizers.

Materials and Methods

Materials

2-Vinyl pyridine (99%, Sigma-Aldrich), Styrene (99%, Alfa Aesar) and deuterated styrene-d8 (98%, Polymer Source Inc.) were stirred over calcium hydride (95%, Millipore-Sigma)) over night, degassed and distilled under vacuum the following day prior to use. Azobisisobutyronitrile (AIBN, 98%, Sigma-Aldrich) was recrystallized from methanol and stored at 0°C before use. 1,4-Dioxane (95%, Sigma-Aldrich) was dried over sodium and distilled prior to use. Tetramethylrhodamine-5-maleimide (85%, Sigma-Aldrich), Methanol (99% Fisher), Diethyl ether (Fischer scientific) and Hexanes (Fischer scientific), Pentaerythritol tetrakis[2-(dodecylthiocarbonothioylthio)-2-2methylpropionate] (97%, Millipore-Sigma) were used as received. Polystyrene (PS) (~280 000g/mol) for adhesion measurement was purchased from Sigma-Aldrich. Poly(2-vinyl pyridine) (200 000g/mol) for adhesion measurement was purchased from Scientific Polymer Product Inc. Deuterated polystyrene (dPS) (285 000 g/mol, Đ=1.12) for neutron reflectivity measurement was purchased from Polymer Source. Inc. Polystyrene (217 000 g/mol, Đ=1.04) for neutron reflectivity measurement was purchased from Polymer Source. Inc. Poly(2-vinyl pyridine) (204 000 g/mol, Đ=1.3) for neutron reflectivity measurement was purchased from Polymer Source. Inc. Polystyrene (13 000 g/mol)-*block*-Poly(2-vinyl pyridine)

(13 000 g/mol) (Đ=1.04) used as linear BCPs for adhesion measurement was purchased from Polymer Source. Inc.

Trilayer preparation for Neutron reflectivity

P2VP homopolymer (204 kg/mol) was dissolved in tetrahydrofuran (THF) and spin-coated onto wafers (~80nm thickness) after filtration. The first layer thickness was measured using ellipsometry and interferometry. Star block copolymers (s-BCPs) were dissolved in toluene (orthogonal solvent to P2VP) at a series of concentrations, resulting in second layer thicknesses of ~5 nm, ~10 nm, and ~15 nm. The total bilayer thickness was measured, and the second layer thickness was calculated by subtracting the first layer thickness. PS homopolymer (271 kg/mol) was dissolved in toluene and spin-coated onto separated glass slides after filtration (~80 nm thickness). The PS film was transferred onto the bilayer samples after scratching the glass edge and transferring it to a water bath. After drying and vacuum treatment, the total layer thickness was measured, yielding the PS layer thickness. The samples were thermally annealed at 178 ℃ under vacuum for 24 hours, followed by slow cooling to room temperature.

Trilayer beam preparation for confocal microscopy and adhesion measurements

PS (280 000 g/mol) beam with 1cm * 5cm *3 mm dimension and P2VP (200 000 g/mol) beam with 1cm * 5cm *2 mm dimension was melt compressed at 155 ℃. Star block copolymers or linear block copolymers was dissolved in toluene and spin-coated onto top of P2VP beam. After drying in vacuum, two beams were joint together under slight pressure at 178 ℃ with nitrogen atmosphere for 2 h, followed by slowly cooling down.

Neutron reflectivity (NR)

Neutron reflectivity (NR) was performed at the Oak Ridge National Laboratory (ORNL) Spallation Neutron Source (SNS) on the Liquids Reflectometer (LR, BL-4B). The scattering vector (q) ranged from 0.008 – 0.2 Å^{-1} was achieved from combination of changing neutron wavelength (λ) between 2.55 Å and 18.5 Å with resolution dq/q =0.028 and incident angle comprising 0.6, 1.18 and 2.35°. The q is defined as $q = \dfrac{4\pi sin(\theta)}{\lambda}$, where θ is scattering angle, λ is neutron wavelength. Direct incident beam was performed to normalize experiment reflectivity data. The experiment was performed at air with room temperature and neutron counts are 720 000 at q range 0.1~0.2 Å to assure good statistical results. The specular reflection was collected. The NR reflectivity was analyzed by Motofit based on Igor Pro.

Grazing-incident small angle neutron scattering (GISANS)

Grazing-incident small angle neutron scattering (GISANS) was performed at ORNL SNS with EQ-SANS instrument at beamline 6 (BL-6).[38] The instrument is a time-of-flight SANS instrument. The sample to detector distance was set to either 1.3 m or 4 m, and the minimum wavelength was set to 7 Å. The shorter sample to detector distance provided a q range of 0-0.3 Å^{-1}, while the longer setting provided a q range of at 0~0.1 Å^{-1}. The samples were mounted on a goniometer that allowed reproducible incident angle to be measured. Exposure time were 1 h~3 h. Data reduction into 2D followed standard procedure that are implemented in the drtsans data reduction software.[39]

Confocal laser scanning fluorescence microscopy (CLSM)

Confocal laser scanning fluorescence microscopy (CLSM) was performed on Nikon A1R25 in the Light Microscopy Facility and Nikon Center of Excellence at the Institute for Applied Life Sciences (IALS) at UMass Amherst. The studies utilized an excitation laser with a wavelength of 561 nm.

Self-consistent field theory (SCFT)

The volume-based degree of polymerization (N) used in SCFT are calculated using MW of the homopolymers and star BCPs used in neutron reflectivity. $N=MW/(\rho*N_A*\text{reference volume})$, where MW is the molecular weight, ρ is the density of PS and P2VP homopolymers, N_A is the Avogadro constant, and 118 $\mathring{A}^3$ is used as the reference volume, the same as the reference volume used to calculate the segmental interaction parameter c. The MW of commercially available PS and P2VP homopolymers are 271,000 g/mol and 204,000 g/mol. N is calculated to be 3666 and 2518 for PS and P2VP homopolymers, using density of 1.04 and 1.14 g/cm³, respectively. [24] N_{PS} is 48 and N_{P2VP} is 40 for each arm for the low MW star BCPs. N_{PS} is 149 and N_{P2VP} is 129 for each arm for high MW star BCPs. The χ between PS and P2VP is taken as 0.108. [31]

The SCFT calculation was performed using the C++ / Cuda version of PSCF package developed by Dorfman and coworkers. [40, 41] The system containing PS and P2VP homopolymers with star copolymers at the interface is modeled as a one-dimensional problem under Cartesian coordinates. The star architecture is conveniently defined using the vertex map in the PSCF package with the following parameter file as an example for the small MW stars. The first column in the 'blocks' section, either 0 or 1, refers to either styrene or 2-vinylpyridine monomer.

The second column, either 48 or 40, refers to the degree of polymerization of each block. The

third and fourth column are the vertex of the beginning and ending of the block. The following

parameter profile defines a four-arm core-shell block copolymer, where each arm contains a PS

block and a P2VP block. The four arms are jointed at the end of the PS blocks with vertex=0.

```
Polymer{

    type    branched

    nBlock  8

    blocks  0  48 0 1

            1  40 1 2

            0  48 0 3

            1  40 3 4

            0  48 0 5

            1  40 5 6

            0  48 0 7

            1  40 7 8

    phi     0.1579

}
```

Phase behaviors of immiscible polymer blends

A blend film of PS/P2VP was prepared by drop-casting a solution onto a Si substrate. The solution comprised a mixture of PS homopolymer (271,000 g/mol) and P2VP homopolymer (204,000 g/mol) in a 70:30 weight ratio, dissolved in THF. Additionally, either 10 wt% or 3 wt% s-BCPs or linear BCPs were added into the mixture as compatibilizers. Following air-drying, the film underwent thermal annealing at 178 ℃ in a vacuum for 24 hours. To remove the P2VP domains, the annealed film was first rinsed with ethanol and subsequently immersed in an ethanol reservoir. The statistical domain size was measured by Polarized Optical Microscopy The final blend film's morphology was examined using an Asylum MFP-3D in tapping mode.

A blend film of PS/P2VP was prepared by drop-casting a solution of mixture of PS homopolymer (271,000 g/mol) and P2VP homopolymer (204,000 g/mol) at 70 wt% to 30 wt% ratio in THF solvent onto Si substrate. 10 wt% or 3 wt% of s-BCPs or linear BCPs was added as compatibilizer. The solution was air-dried, followed by thermal annealing at 178 ℃ under vacuum for 24 hours. The resulted blend film was first rinsed by ethanol solvent then immersed in ethanol reservoir to fully remove the P2VP domain. The resulted blend film was measured on Asylum MFP-3D in tapping mode for detailed morphology.

Adhesion measurements

To induce controlled cracking at the interface between two beams comprising star block copolymers or linear block copolymers with varied concentrations, a razor blade was gently inserted. The crack length was subsequently measured after one day to allow for equilibrium to be reached. The Young's modulus values used for the beams were 3000 MPa for PS and 3500

MPa for P2VP. [24] The thickness of the PS beam was 3 mm, while the P2VP beam had a thickness of 2 mm. The equilibrium crack length was measured after the one-day insertion period.

AUTHOR INFORMATION

Corresponding Author

Thomas P. Russell (russell@mail.pse.umass.edu)

Author Contributions

‡ Z.C and C.S contributed equally to this work. T.P.R conceptualize this research. Z.C performed sample preparation and NR, GISANS, CLSM and ADCB experiments. C.S. synthesized star block copolymers and assisted NR experiments. M.H performed SCFT simulation and assisted GISANS experiments. H.W assisted NR experiments. W.T.H and W.B assisted GIANS experiments. Z.C wrote original manuscript. All authors revised the manuscript. All authors have given approval to the final version of the manuscript.

SUPPORTING INFORMATION

Synthesis and characterization of s-BCPs; SAXS profile of s-BCPs; Neutron reflectivity fitting for different contrasts; Confocal laser scanning fluorescence microscopy of PS beam; SCFT calculation for determination of CMC; Simulated neutron reflectivity assuming s-BCPs multilayer at interface; GISANS for out-of-plane and in-plane interference; Segmental density distribution solved from neutron reflectivity with varied MW and interlayer thickness; Segmental density distribution solved from neutron reflectivity with multiple contrast samples ; SCFT calculation for probing s-BCP interfacial configuration in terms of segment (block) distribution and junction point distribution with variation of MW and interlayer thickness, and the

comparison with linear BCPs; POM results of PS/P2VP blend with addition of BCPs; Summarized tables for interfacial assembly information on star BCPs and linear BCPs, solved from neutron reflectivity and SCFT.

ACKNOWLEDGMENT

REFERENCES

(1) Wu, S. *Polymer Interface and Adhesion*; 2017. DOI: 10.1201/9780203742860.

(2) Awaja, F.; Gilbert, M.; Kelly, G.; Fox, B.; Pigram, P. J. Adhesion of polymers. *Progress in Polymer Science* **2009**, *34* (9), 948-968. DOI: 10.1016/j.progpolymsci.2009.04.007.

(3) Dorigato, A. Recycling of polymer blends. *Advanced Industrial and Engineering Polymer Research* **2021**, *4* (2), 53-69. DOI: 10.1016/j.aiepr.2021.02.005.

(4) Khanna, V. K. Adhesion–delamination phenomena at the surfaces and interfaces in microelectronics and MEMS structures and packaged devices. *Journal of Physics D: Applied Physics* **2010**, *44* (3). DOI: 10.1088/0022-3727/44/3/034004.

(5) Guchait, A.; Saxena, A.; Chattopadhyay, S.; Mondal, T. Influence of Nanofillers on Adhesion Properties of Polymeric Composites. *ACS Omega* **2022**, *7* (5), 3844-3859. DOI: 10.1021/acsomega.1c05448 From NLM PubMed-not-MEDLINE.

(6) Wei, B.; Liu, J.; Ouyang, L.; Kuo, C. C.; Martin, D. C. Significant enhancement of PEDOT thin film adhesion to inorganic solid substrates with EDOT-acid. *ACS Appl Mater Interfaces* **2015**, *7* (28), 15388-15394. DOI: 10.1021/acsami.5b03350 From NLM Medline.

(7) Russell, T. P. Copolymers at surfaces and interfaces. *Current Opinion in Colloid & Interface Science* **1996**, *1* (1), 107-115. DOI: 10.1016/s1359-0294(96)80051-3.

(8) Bernard, B.; Brown, H. R.; Hawker, C. J.; Kellock, A. J.; Russell, T. P. Adhesion of Polymer Interfaces Reinforced with Random and Diblock Copolymers as a Function of Geometry. *Macromolecules* **1999**, *32* (19), 6254-6260. DOI: 10.1021/ma970125x.

(9) Pellegrini, N. N.; Sikka, M.; Satija, S. K.; Winey, K. I. Segregation of a Random Copolymer from Miscible Blends. *Macromolecules* **1997**, *30* (21), 6640-6644. DOI: 10.1021/ma970586i.

(10) Korley, L. T. J.; Epps, T. H., 3rd; Helms, B. A.; Ryan, A. J. Toward polymer upcycling-adding value and tackling circularity. *Science* **2021**, *373* (6550), 66-69. DOI: 10.1126/science.abg4503 From NLM PubMed-not-MEDLINE.

(11) Epps, T. H., 3rd; Korley, L. T. J.; Yan, T.; Beers, K. L.; Burt, T. M. Sustainability of Synthetic Plastics: Considerations in Materials Life-Cycle Management. *JACS Au* **2022**, *2* (1), 3-11. DOI: 10.1021/jacsau.1c00191 From NLM PubMed-not-MEDLINE.

(12) Kwon, D. Three ways to solve the plastics pollution crisis. *Nature* **2023**, *616* (7956), 234-237. DOI: 10.1038/d41586-023-00975-5 From NLM Medline.

(13) Schyns, Z. O. G.; Shaver, M. P. Mechanical Recycling of Packaging Plastics: A Review. *Macromol Rapid Commun* **2021**, *42* (3), e2000415. DOI: 10.1002/marc.202000415 From NLM Medline.

(14) Maris, J.; Bourdon, S.; Brossard, J.-M.; Cauret, L.; Fontaine, L.; Montembault, V. Mechanical recycling: Compatibilization of mixed thermoplastic wastes. *Polymer Degradation and Stability* **2018**, *147*, 245-266. DOI: 10.1016/j.polymdegradstab.2017.11.001.

(15) Macosko, C. W.; Jeon, H. K.; Hoye, T. R. Reactions at polymer–polymer interfaces for blend compatibilization. *Progress in Polymer Science* **2005**, *30* (8-9), 939-947. DOI: 10.1016/j.progpolymsci.2005.06.003.

(16) Shull, K. R.; Winey, K. I.; Thomas, E. L.; Kramer, E. J. Segregation of block copolymer micelles to surfaces and interfaces. *Macromolecules* **2002**, *24* (10), 2748-2751. DOI: 10.1021/ma00010a017.

(17) Self, J. L.; Zervoudakis, A. J.; Peng, X.; Lenart, W. R.; Macosko, C. W.; Ellison, C. J. Linear, Graft, and Beyond: Multiblock Copolymers as Next-Generation Compatibilizers. *JACS Au* **2022**, *2* (2), 310-321. DOI: 10.1021/jacsau.1c00500 From NLM PubMed-not-MEDLINE.

(18) Klimovica, K.; Pan, S.; Lin, T. W.; Peng, X.; Ellison, C. J.; LaPointe, A. M.; Bates, F. S.; Coates, G. W. Compatibilization of iPP/HDPE Blends with PE-g-iPP Graft Copolymers. *ACS Macro Lett* **2020**, *9* (8), 1161-1166. DOI: 10.1021/acsmacrolett.0c00339 From NLM PubMed-not-MEDLINE.

(19) Mah, A. H.; Afzali, P.; Qi, L.; Pesek, S.; Verduzco, R.; Stein, G. E. Bottlebrush Copolymer Additives for Immiscible Polymer Blends. *Macromolecules* **2018**, *51* (15), 5665-5675. DOI: 10.1021/acs.macromol.8b00719.

(20) Ren, J. M.; McKenzie, T. G.; Fu, Q.; Wong, E. H.; Xu, J.; An, Z.; Shanmugam, S.; Davis, T. P.; Boyer, C.; Qiao, G. G. Star Polymers. *Chem Rev* **2016**, *116* (12), 6743-6836. DOI: 10.1021/acs.chemrev.6b00008 From NLM Medline.

(21) Huang, K.; Johnson, M.; Rzayev, J. Synthesis of Degradable Organic Nanotubes by Bottlebrush Molecular Templating. *ACS Macro Lett* **2012**, *1* (7), 892-895. DOI: 10.1021/mz3002287 From NLM PubMed-not-MEDLINE.

(22) Heise, A.; Hedrick, J. L.; Frank, C. W.; Miller, R. D. Starlike Block Copolymers with Amphiphilic Arms as Models for Unimolecular Micelles. *Journal of the American Chemical Society* **1999**, *121* (37), 8647-8648. DOI: 10.1021/ja984456g.

(23) Carrillo, J. Y.; Chen, Z.; Premadasa, U. I.; Steinmetz, C.; Coughlin, E. B.; Doughty, B.; Russell, T. P.; Sumpter, B. G. Assembly of polyelectrolyte star block copolymers at the oil-water interface. *Nanoscale* **2023**, *15* (3), 1042-1052. DOI: 10.1039/d2nr05113c From NLM PubMed-not-MEDLINE.

(24) Creton, C.; Kramer, E. J.; Hui, C. Y.; Brown, H. R. Failure mechanisms of polymer interfaces reinforced with block copolymers. *Macromolecules* **2002**, *25* (12), 3075-3088. DOI: 10.1021/ma00038a010.

(25) Russell, T. P.; Anastasiadis, S. H.; Menelle, A.; Felcher, G. P.; Satija, S. K. Segment density distribution of symmetric diblock copolymers at the interface between two homopolymers as revealed by neutron reflectivity. *Macromolecules* **2002**, *24* (7), 1575-1582. DOI: 10.1021/ma00007a020.

(26) Eagan, J. M.; Xu, J.; Di Girolamo, R.; Thurber, C. M.; Macosko, C. W.; LaPointe, A. M.; Bates, F. S.; Coates, G. W. Combining polyethylene and polypropylene: Enhanced performance with PE/iPP multiblock polymers. *Science* **2017**, *355* (6327), 814-816. DOI: 10.1126/science.aah5744 From NLM PubMed-not-MEDLINE.

(27) Russell, T. P.; Menelle, A.; Hamilton, W. A.; Smith, G. S.; Satija, S. K.; Majkrzak, C. F. Width of homopolymer interfaces in the presence of symmetric diblock copolymers. *Macromolecules* **2002**, *24* (20), 5721-5726. DOI: 10.1021/ma00020a036.

(28) Sun, Z.; Zhang, W.; Hong, S.; Chen, Z.; Liu, X.; Xiao, S.; Coughlin, E. B.; Russell, T. P. Using block copolymer architecture to achieve sub-10 nm periods. *Polymer* **2017**, *121*, 297-303. DOI: 10.1016/j.polymer.2017.06.007.

(29) Perrier, S. 50th Anniversary Perspective: RAFT Polymerization—A User Guide. *Macromolecules* **2017**, *50* (19), 7433-7447. DOI: 10.1021/acs.macromol.7b00767.

(30) Russell, T. P. X-ray and neutron reflectivity for the investigation of polymers. *Materials Science Reports* **1990**, *5* (4), 171-271. DOI: 10.1016/s0920-2307(05)80002-7.

(31) Dai, K. H.; Norton, L. J.; Kramer, E. J. Equilibrium Segment Density Distribution of a Diblock Copolymer Segregated to the Polymer/Polymer Interface. *Macromolecules* **2002**, *27* (7), 1949-1956. DOI: 10.1021/ma00085a045.

(32) Pfeifer, S.; Lutz, J. F. A facile procedure for controlling monomer sequence distribution in radical chain polymerizations. *J Am Chem Soc* **2007**, *129* (31), 9542-9543. DOI: 10.1021/ja0717616 From NLM Medline.

(33) Zamfir, M.; Lutz, J.-F. Ultra-precise insertion of functional monomers in chain-growth polymerizations. *Nature Communications* **2012**, *3* (1), 1138. DOI: doi.org/10.1038/ncomms2151.

(34) Hu, M.; Li, X.; Heller, W. T.; Bras, W.; Rzayev, J.; Russell, T. P. Using Grazing-Incidence Small-Angle Neutron Scattering to Study the Orientation of Block Copolymer Morphologies in Thin Films. *Macromolecules* **2023**. DOI: 10.1021/acs.macromol.2c02415.

(35) Creton, C.; Kramer, E. J.; Hadziioannou, G. Critical molecular weight for block copolymer reinforcement of interfaces in a two-phase polymer blend. *Macromolecules* **2002**, *24* (8), 1846-1853. DOI: 10.1021/ma00008a023.

(36) Yang, J.; Bai, R.; Chen, B.; Suo, Z. Hydrogel Adhesion: A Supramolecular Synergy of Chemistry, Topology, and Mechanics. *Advanced Functional Materials* **2019**, *30* (2). DOI: 10.1002/adfm.201901693.

(37) Bryson, K. C.; Löbling, T. I.; Müller, A. H. E.; Russell, T. P.; Hayward, R. C. Using Janus Nanoparticles To Trap Polymer Blend Morphologies during Solvent-Evaporation-Induced Demixing. *Macromolecules* **2015**, *48* (12), 4220-4227. DOI: 10.1021/acs.macromol.5b00640.

(38) Heller, W. T.; Cuneo, M.; Debeer-Schmitt, L.; Do, C.; He, L.; Heroux, L.; Littrell, K.; Pingali, S. V.; Qian, S.; Stanley, C.; et al. The suite of small-angle neutron scattering instruments at Oak Ridge National Laboratory. *Journal of Applied Crystallography* **2018**, *51* (2), 242-248. DOI: 10.1107/s1600576718001231.

(39) Heller, W. T.; Hetrick, J.; Bilheux, J.; Calvo, J. M. B.; Chen, W.-R.; DeBeer-Schmitt, L.; Do, C.; Doucet, M.; Fitzsimmons, M. R.; Godoy, W. F.; et al. drtsans: The data reduction toolkit for small-angle neutron scattering at Oak Ridge National Laboratory. *SoftwareX* **2022**, *19*. DOI: 10.1016/j.softx.2022.101101.

(40) Cheong, G. K.; Chawla, A.; Morse, D. C.; Dorfman, K. D. Open-source code for self-consistent field theory calculations of block polymer phase behavior on graphics processing units. *Eur Phys J E Soft Matter* **2020**, *43* (2), 15. DOI: 10.1140/epje/i2020-11938-y From NLM PubMed-not-MEDLINE.

(41) Arora, A.; Qin, J.; Morse, D. C.; Delaney, K. T.; Fredrickson, G. H.; Bates, F. S.; Dorfman, K. D. Broadly Accessible Self-Consistent Field Theory for Block Polymer Materials Discovery. *Macromolecules* **2016**, *49* (13), 4675-4690. DOI: 10.1021/acs.macromol.6b00107.